

Self-amplifying spin measurement in a long-lived spin-squeezed state

Meng-Zi Huang¹, Jose Alberto de la Paz², Tommaso Mazzoni², *

Konstantin Ott^{1,†}, Alice Sinatra¹, Carlos L. Garrido Alzar², and Jakob Reichel^{1‡}

¹*Laboratoire Kastler Brossel, ENS-Université PSL, CNRS, Sorbonne Université,*

Collège de France, 24 rue Lhomond, 75005 Paris, France

²*LNE-SYRTE, Observatoire de Paris-Université PSL, CNRS,*

Sorbonne Université, 61 Avenue de l'Observatoire, 75014 Paris, France

(Dated: July 3, 2020)

Using the platform of a trapped-atom clock on a chip, we have generated spin-squeezed states with up to 8.1(9) dB of metrological squeezing in a cloud of 2×10^4 ultracold alkali atoms by quantum nondemolition (QND) measurement in a fiber Fabry-Perot microcavity. Observing the time evolution of the squeezed state on unprecedented timescales of more than one second reveals a surprising measurement amplification effect in the final measurement of the spin state. It results from a subtle interplay between the spin dynamics of interacting indistinguishable particles and energy-dependent cavity coupling and leads to an increased cavity shift per spin, and thus to a higher signal per photon read out. Metrological spin squeezing is preserved for 1 s. Both results open up encouraging perspectives for squeezing-enhanced atomic clocks in a metrologically relevant stability regime.

I. INTRODUCTION

Spin squeezing in atomic ensembles [1–4] is a fascinating manifestation of many-particle entanglement as well as one of the most promising quantum technologies. By using entanglement to reduce the quantum projection noise in a collection of atomic spins, spin squeezing removes a limit that has already been reached in state-of-the-art atomic fountain clocks [5] and is expected to impact optical lattice clocks [6] and atomic sensors [7–9] in the near future. Ground-breaking experiments have demonstrated methods to create spin-squeezed states [10–18] and have even demonstrated squeezing-enhanced clocks and magnetometers in proof-of-principle experiments [18–21]. In all experiments so far, however, the coherence time of the atomic superpositions was short (typically less than 10 ms), while interrogation times in real clocks and sensors are often ten or hundred times longer. How the squeezed states evolve on these timescales is a question that experiments have not yet been able to address. Besides its practical importance, the physics of this time evolution is an interesting question in its own right. Long coherent evolution acts like a magnifying glass for atomic interactions, often leading to surprising effects. In a trapped ultracold gas, cold collisions are the most prominent interactions. They are responsible for one of the largest contributions to the uncertainty of Cesium and Rubidium fountain clocks [22], and also need to be taken into account in fermionic lattice clocks [23]. But collisions can also have beneficial effects. In suitable regimes of density and temperature, they lead to the so-called identical spin rotation effect (ISRE) [24]

that prevents spins from dephasing [25, 26]. Similar spin-locking mechanisms also exist in optical lattice clocks [27] and degenerate Fermi gases [28]. How do these interacting many-body systems evolve when the initial state is no longer a product state of N independent particles, but an entangled state with quantum correlations between their spin degrees of freedom?

Here we investigate measurement-based spin squeezing in an optical cavity [12] in the setting of a trapped-atom clock on a chip [25, 29], where the coherence lifetime is about 20 s and cold collisions are known to play an important role. We observe conditional spin squeezing by cavity QND measurement, reaching 8.1(9) dB metrological gain with respect to the standard quantum limit (SQL). Investigating how the squeezed state evolves over a duration of two seconds, we observe a manifestation of the interplay between the squeezing measurement and spin-exchange collisions which results in an amplification of the squeezing measurement (i.e., increases the signal per photon) on a timescale of hundreds of milliseconds. Metrological squeezing is preserved for times up to one second. We develop a simple model that gives an intuitive understanding of the amplification effect, based on a correlation between spin and atom-cavity coupling which arises due to the exchange interaction. The model is confirmed by a direct measurement of spin-temperature correlation. These results show a clear prospect for spin-squeezed clock improvement in the metrologically relevant regime of compact microwave clocks with $10^{-13} \text{ s}^{-1/2}$ stability in the near future. They also highlight a class of spin interactions that is likely to be relevant for many future squeezing-enhanced clocks and sensors.

* Present address: Muquans SAS, Talence, France

† Present address: VITRONIC Dr.-Ing. Stein Bildverarbeitungssysteme GmbH, Wiesbaden, Germany

‡ jakob.reichel@ens.fr

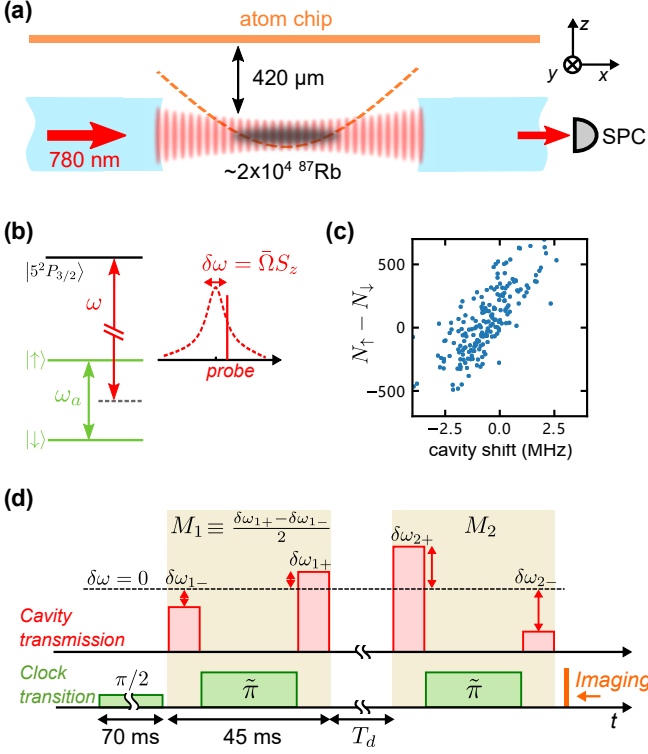


FIG. 1. (a) Experimental setup. ^{87}Rb atoms are magnetically trapped inside the Fabry-Pérot cavity. The dashed orange curve indicates the magnetic trapping potential created by the atom chip. Transmitted photons are collected by a single photon counter (SPC). Absorption images are taken along \hat{y} . Cavity locking light at 1560 nm is not shown. (b) Energy level structure and cavity probing scheme. (c) Typical data of cavity measurement versus atom number measurement by absorption imaging, here for $N = 2.3(1) \times 10^4$ atoms. Imaging noise amounts to $\Delta_{\text{img}}(N_\uparrow - N_\downarrow) \sim 100$, comparable to the SQL, limiting the correlation. (d) Experimental sequence with two composite cavity measurements M_1 and M_2 for squeezing verification and for observing the amplification effect. Green boxes represent pulses on the clock transition, and red boxes cavity probe transmission, from which $\delta\omega_\pm$ are deduced. The delay T_d between measurements can vary from a few ms to 2 s. $\tilde{\pi}$ denotes a composite π pulse.

II. EXPERIMENTAL SETTING

Our experiment is similar to the trapped-atom clock on a chip (TACC) described in [25, 29], but additionally contains a fiber Fabry-Pérot cavity [30]. An ensemble of $N \sim 2 \times 10^4$ ^{87}Rb atoms is magnetically trapped inside this cavity using an atom chip (Fig. 1(a)). The trap is cigar-shaped with frequencies $\{\omega_x, \omega_y, \omega_z\}/2\pi \approx \{7.5, 122, 113\}$ Hz, with the cavity axis along \hat{x} . The atom cloud has temperatures $T \approx 200$ nK transversely (\hat{y} and \hat{z}) and $T_x \approx 140$ nK longitudinally, leading to $1/e$ cloud dimensions of $\sigma_x \sim 100$ μm and $\sigma_{y,z} \sim 9$ μm and an average density of $\bar{n} \sim 1.6 \times 10^{11}$ cm $^{-3}$. The $1/e$ trap lifetime is 3.0(1) s, limited by a small leak in the vacuum system. Forward (kinetic-energy preserving) collisions

lead to a spin-exchange rate $\omega_{\text{ex}}/2\pi = 2\hbar|a_{\uparrow\downarrow}|\bar{n}/m \sim 1$ Hz, where $a_{\uparrow\downarrow} \approx 98.09a_0$, with $a_0 = 0.0529$ nm, is the relevant scattering length, and m is the atomic mass. Lateral collisions occur with a still lower rate $\gamma_c = (32\sqrt{\pi}/3)a_{\uparrow\downarrow}^2\bar{n}v_T \sim 0.3$ Hz, where v_T is the thermal velocity $v_T \approx \sqrt{k_B T/m}$ and k_B is the Boltzmann constant. Therefore, the atom cloud is in the so-called Knudsen regime where the collision rate is lower than the trapping frequencies $\omega_{y,z} \gg \omega_x > \omega_{\text{ex}} > \gamma_c$. Each atom preserves its motional state over many oscillations in the trap.

The hyperfine states $|\downarrow\rangle \equiv |F = 1, m_F = -1\rangle$ and $|\uparrow\rangle \equiv |F = 2, m_F = 1\rangle$ are used as clock states [25, 31]. An exponential fit to time-domain Ramsey fringes with a coherent spin state (CSS) yields a phase coherence time on the order of 20 s, longer than the lifetime of the sample due to background collisions. Used as a clock with standard Ramsey interrogation and non-squeezed atoms, the experiment currently reaches a fractional frequency stability of 6.5×10^{-13} s $^{-1/2}$.

We consider the collective spin vector $\hat{\mathbf{S}} = \sum_i^N \hat{\mathbf{s}}_i$ of N spin- $\frac{1}{2}$'s, with $\hat{\mathbf{s}}_i = \frac{1}{2}\{\hat{\sigma}_x^{(i)}, \hat{\sigma}_y^{(i)}, \hat{\sigma}_z^{(i)}\}$ where $\hat{\sigma}_{x,y,z}^{(i)}$ are Pauli matrices for the i -th atom. The z component represents the population difference $\hat{S}_z = (\hat{N}_\uparrow - \hat{N}_\downarrow)/2$, where \hat{N}_\uparrow and \hat{N}_\downarrow are the number operators of $|\downarrow\rangle$ and $|\uparrow\rangle$, respectively. (We will use symbols without hat to denote a measurement outcome.) For a CSS, the fluctuations in measurements of \hat{S}_z are given by the SQL: $(\Delta S_z)^2|_{\text{CSS}} = N/4$, where Δ denotes the standard deviation. Spin squeezing is generated by a QND measurement of the collective spin observable \hat{S}_z via the frequency shift $\delta\omega$ that it induces to an off-resonant optical cavity [12]. The cavity has a mode waist ($1/e$ radius) $w_0 = 13.6$ μm, length $L = 1215(20)$ μm and linewidth (FWHM) $\kappa/2\pi = 45.8(6)$ MHz. It is tuned midway between the 780 nm D2 transitions $|\downarrow\rangle \rightarrow 5P_{3/2}$ and $|\uparrow\rangle \rightarrow 5P_{3/2}$, such that to good approximation $\delta\omega = \bar{\Omega}S_z$ where $\bar{\Omega} = \sum_i^N \Omega_i/N$ is the ensemble-averaged shift per spin flip and Ω_i is the coupling strength of the i -th atom. The value $\bar{\Omega} = 2\pi \times 16.2(3)$ kHz has an uncertainty limited by the atom temperature, and is determined experimentally by measuring the cavity shift after preparing the ensemble in coherent states with different $\langle S_z \rangle$ (Appendix A 2). In the following experiments, we prepare a CSS of $\langle S_z \rangle = 0$ with a $\pi/2$ pulse on the clock transition. $\delta\omega$ is measured with a probe laser which is blue detuned from the cavity resonance by $\sim \kappa/2$ (Fig. 1(b)). We detect the transmitted photons using a single-photon counter, with an overall detection efficiency $\eta = 0.63(2)$. N_\uparrow and N_\downarrow are also measured by absorption imaging after time-of-flight (TOF). We have verified that both measurements agree to within the noise of the absorption imaging, which is close to the SQL (Fig. 1(c)).

The inhomogeneity of the single-atom coupling Ω_i will play a crucial role in the experiments of Sec. III B. It is predominantly in the transverse directions, where the cavity intensity profile varies by $\sim 34\%$ of its maximum

over the $1/e$ radius of the atomic cloud. Along the cavity axis (\hat{x}), the standing wave potential generated by the probe and by the 1560 nm locking light are both below 20 nK, so that atomic motion largely averages out the inhomogeneity. In order to reduce inhomogeneity-induced dephasing, we use a fixed probe pulse duration equal to the vertical trap period, $\tau_p = 8.85$ ms = $2\pi/\omega_z \approx 2\pi/\omega_y$. Thus, to first approximation, Ω_i only depends on an atom's transverse thermal energy and remains constant until a lateral collision occurs (Appendix B). The remaining inhomogeneity between atoms with different motional energies is further suppressed by employing a spin echo sequence, as in previous experiments [12, 15]. A complete cavity measurement is then composed of two cavity probe pulses separated by a π pulse on the clock transition (Fig. 1(d)). The measured S_z is deduced from the cavity shifts $\delta\omega_{\pm}$ of the two probe pulses, and we define a cavity measurement $M \equiv (\delta\omega_+ - \delta\omega_-)/2$.

III. RESULTS

A. Spin squeezing by QND measurement

We first investigate the metrological spin squeezing generated by our cavity QND measurement. As shown in Fig. 1(d), we start with all atoms in $|\downarrow\rangle$ and apply a $\pi/2$ pulse on the clock transition to prepare a CSS on the equator of the Bloch sphere. A composite cavity measurement M_1 is performed to measure S_z . A second measurement M_2 after a delay $T_d = 6$ ms serves to verify the measurement uncertainty and spin squeezing. Noise is quantified from the variance of 200 repetitions of this sequence. First, we perform this protocol with an empty cavity to determine the noise floor (Fig. 2(a), open black circles). The result is close to the photon shot noise (PSN) of the detected photons, given by $(\Delta M_l^{\text{PSN}})^2 \approx \kappa^2/(4\langle n_l \rangle)$, where $\langle n_l \rangle$ is the average number of detected photons per measurement ($l = 1, 2$). For the atom number $N = 2.3(1) \times 10^4$ used here, the PSN falls below the SQL for $\langle n_1 \rangle \gtrsim 1000$ detected photons, allowing for spin noise reduction by the cavity measurement.

A QND measurement produces “conditional squeezing”: M_1 yields a different result every time, following the quantum fluctuations of the CSS. The squeezing manifests itself in the correlation with the second measurement M_2 , which for a squeezed state agrees with M_1 to better than the quantum projection noise [4]. For two identical QND measurements, the spin noise is quantified by $\text{Var}(M_1 - M_2)$ and the measurement noise has a lower limit given by the PSN, $(\Delta M_1^{\text{PSN}})^2 + (\Delta M_2^{\text{PSN}})^2$. More generally, the spin noise reduction can still be fully characterized from the correlation between M_1 and M_2 even if M_1 and M_2 are not identical, say if they have different probe intensities, or due to other systematic effects. We will infer the conditional spin noise $(\Delta S_z)^2|_{M_1}$ from the conditional noise $\text{Var}(M_1 - M_2/\alpha)$ where α is

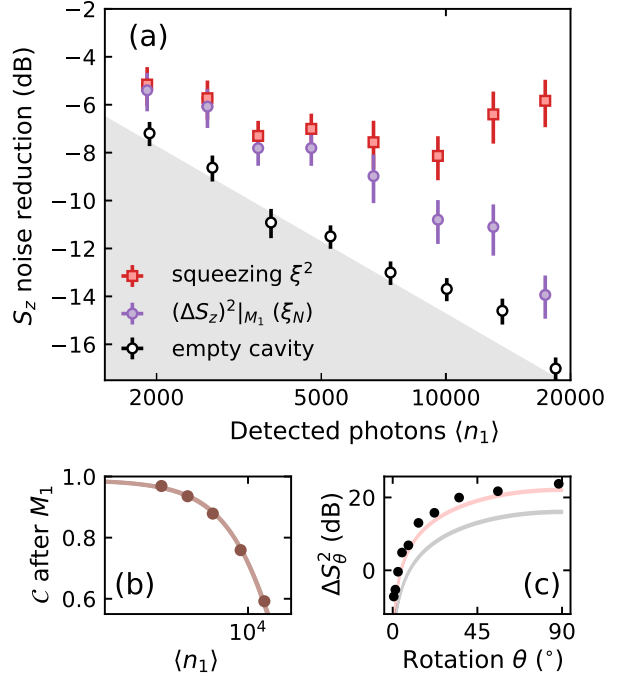


FIG. 2. (a) Conditional squeezing results for $N = 2.3(1) \times 10^4$ atoms. Variance values are normalized to the SQL ($N/4$) and expressed in dB. The empty cavity measurement (open black circles) approaches the PSN limit (boundary of the shaded zone). Number squeezing $(\Delta S_z)^2|_{M_1}$ (solid purple circles) is deduced from the conditional noise $\text{Var}(M_1 - M_2/\alpha)$ (see text), with α determined from each dataset ($0.9 < \alpha < 1.7$ for these data). Here, N is obtained from absorption imaging, which gives a conservative estimate of the achieved squeezing in an inhomogeneous system [32] (Appendix B). Accounting for the independently measured coherence shown in (b), we obtain the metrological squeezing (red squares). It reaches 8.1(9) dB for $9.6(2) \times 10^3$ photons. Error bars indicate 1σ confidence and are obtained with a bootstrapping method. (b) Ramsey contrast C as a function of measurement strength. The curve is a fit to $C = \exp[-\langle n_1 \rangle/\gamma_1 - (\langle n_1 \rangle/\gamma_2)^2]$, with two decay constants γ_1 and γ_2 (Appendix C 1). Its thickness indicates fit uncertainty. (c) Spin noise tomography at $\langle n_1 \rangle = 8.9(2) \times 10^3$ measured by inserting between M_1 and M_2 a rotation θ around $\langle \hat{S} \rangle$. The gray curve represents the theoretical minimum uncertainty state, while the pink curve takes into account the phase noise induced by the PSN of M_1 (see text). The thickness of the curves indicates 1σ uncertainty.

the number that minimizes the variance normalized to the PSN limit, which is $(\Delta M_1^{\text{PSN}})^2 + (\Delta M_2^{\text{PSN}})^2/\alpha^2$ in this case (Appendix C 2).

Considering that we are interested in the state after M_1 , it is legitimate to subtract the PSN of M_2 (but not that of M_1), so that we obtain

$$(\Delta S_z)^2|_{M_1} = [\text{Var}(M_1 - M_2/\alpha) - (\Delta M_2^{\text{PSN}})^2/\alpha^2] / \bar{\Omega}^2. \quad (1)$$

This is an upper bound for $(\Delta S_z)^2$ because we do not subtract other noise such as technical noise in M_2 .

In Fig. 2(a) (purple circles), we show this condi-

tional spin noise as a function of the measurement strength of M_1 . It is normalized to the SQL to give the number squeezing $\xi_N^2 = 4(\Delta S_z)^2|_{M_1}/N$ [1]. To assess the metrological squeezing $\xi^2 = N(\Delta S_z)^2/|\langle \hat{\mathbf{S}} \rangle|^2 = 4(\Delta S_z)^2|_{M_1}/(NC^2)$, which characterizes the enhancement in angular resolution on the Bloch sphere with respect to the SQL [2], we also need to measure the Ramsey fringe contrast $\mathcal{C} = 2|\langle \hat{\mathbf{S}} \rangle|/N$. We do this by applying a second $\pi/2$ pulse with a variable phase after M_1 and then measuring S_z by imaging for each phase value (Fig. 2(b)). The contrast decay for increasing photon number is dominated by the imperfect light-shift cancellation in the spin-echo. We obtain an optimum metrological squeezing of 8.1(9) dB.

To better characterize the squeezed state, we have also performed spin noise tomography [12, 16] by inserting a pulse on the clock transition between M_1 and M_2 to rotate the noise distribution around $\langle \hat{\mathbf{S}} \rangle$ (Fig. 2(b), Appendix C 3). The data show an anti-squeezing 7.4 dB (at 90° rotation) above the minimum uncertainty state (gray curve), mostly due to the shot-to-shot phase noise caused by the PSN in M_1 (red curve).

B. Amplification of cavity measurement

The phase coherence time of approximately 20 s in our experiment is longer than all other relevant timescales. This makes it possible to observe the evolution of the spin-squeezed states over much longer timescales than in previous experiments. We do so by performing the verification measurement M_2 after a longer time T_d . As shown in Fig. 3(a), the correlation between the results M_1 and M_2 persists for more than one second. For all times, their relationship remains linear to a good approximation, $M_2 \approx \alpha M_1$, but surprisingly, α evolves over time, as shown in Fig. 3(b): M_2 is amplified with respect to M_1 , with an amplification factor α that reaches a maximum of $\alpha \approx 4$ at 300 ms and remains significantly above 1 up to $T_d \approx 800$ ms. By performing absorption imaging, we have confirmed that S_z itself does not measurably evolve after M_1 .

In Fig. 3(c) we quantify the correlation between M_1 and M_2 with the amplification taken into account: $\text{Var}(M_1 - M_2/\alpha)$. This must be compared with the relevant PSN limit $(\Delta M_1^{\text{psn}})^2 + (\Delta M_2^{\text{psn}})^2/\alpha^2$ (dashed curve). The correlation remains very close to this limit for more than 500 ms. It gradually deteriorates for longer times, but remains significantly below the value expected for two uncorrelated measurements at the SQL (dotted curve), showing that correlation persists even at the longest times. Note that, due to the amplification, the noise contribution from M_2 can be significantly smaller than the PSN of M_1 , in spite of the two measurements using the same average photon numbers.

Some insight into the mechanism causing this amplification can be obtained from a simple spin model, illustrated in Fig. 4, which takes into account the exchange

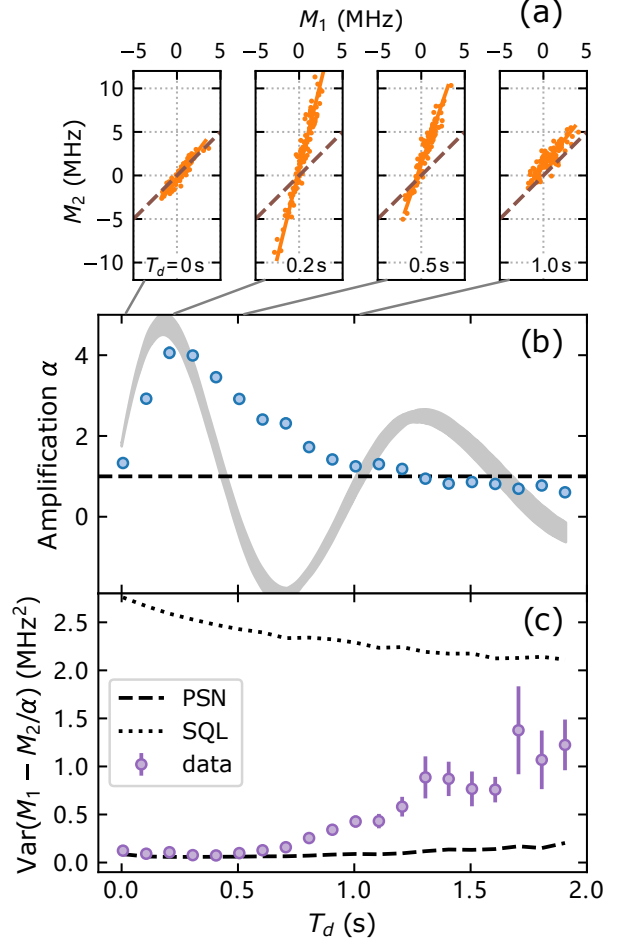


FIG. 3. (a) Raw data of M_2 versus M_1 at $T_d = 0, 0.2, 0.5, 1$ s, respectively. Dashed lines indicate $M_2 = M_1$ (as for $T_d = 0$). The slope of a linear fit (solid lines) gives the amplification factor in (b). (b) Amplification factor α (blue circles) as a function of time. The gray curve is the result of a semi-classical Monte Carlo simulation (width representing the uncertainty), which captures the initial dynamics but fails to reproduce the strong damping of the evolution (see text and Appendix E). The dashed line indicates no amplification. (c) Conditional noise $\text{Var}(M_1 - M_2/\alpha)$ (purple circles). The PSN limit $(\Delta M_1^{\text{psn}})^2 + (\Delta M_2^{\text{psn}})^2/\alpha^2$ (dashed curve) and the SQL from two uncorrelated measurements $\bar{\Omega}^2 N/2$ (dotted curve) are shown for comparison. These curves are calculated taking into account the measured atom loss, which is significant for these long evolution times. Error bars represent 1σ confidence.

interaction and the energy-dependent variation of cavity coupling, but not the quantum fluctuations or correlations. Spin dynamics is started by the first measurement: due to the inhomogeneity in the cavity coupling, the phase shift induced by the cavity field slightly differs between atoms, leading to a dephasing. This kind of dephasing is present to some degree in all light-based squeezing experiments. (As it occurs in the plane perpendicular to the squeezed axis, its impact on the metrological enhancement is limited as long as the phase deviation

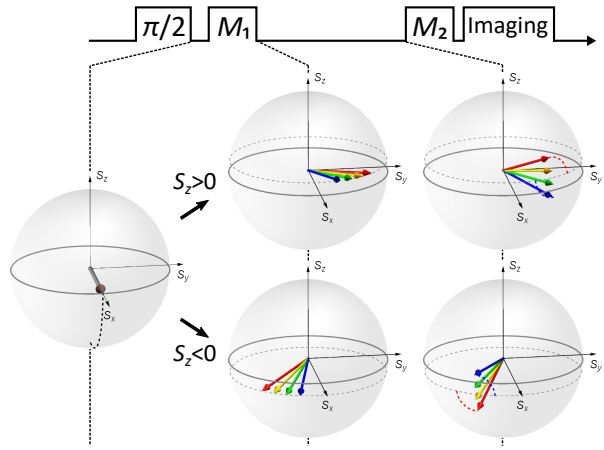


FIG. 4. Intuitive picture of the amplification effect in the single-atom Bloch sphere. Atoms are prepared in phase by the $\pi/2$ pulse (left column). The center column shows the situation just after the measurement M_1 . Two cases are shown, one where the measurement result was $S_z > 0$ (upper row) and one where it was $S_z < 0$ (lower row). Each arrow depicts a single atom, with its color representing the coupling Ω_i , which depends on motional energy (blue: higher energy, $\Omega_i < \bar{\Omega}$; red: lower energy, $\Omega_i > \bar{\Omega}$). Cold, well-coupled atoms (red arrows) lead when $S_z > 0$ (upper row), and lag when $S_z < 0$ (lower row). During evolution under ISRE (right column), individual spins rotate around their sum, acquiring different individual s_z components while total S_z is conserved. For times shorter than $\omega_{\text{ex}}/2$, well-coupled atoms rotate above (below) the average if $S_z > 0$ ($S_z < 0$). As these atoms make an above-average contribution to the cavity shift, the second measurement performed at this stage yields an amplified signal. Note that if $S_z = 0$ is measured, atoms remain in phase (thick gray arrow) and no spin dynamics occurs.

to be measured is not too large [33].) With the composite measurement scheme (Fig. 1(d)), the two probe pulses compensate each other's dephasing up to the imbalance in transmission that depends on the measured S_z . Here, we only need to consider the relative phase δ_i of atom i with respect to the mean phase shift. Well-coupled atoms ($\Omega_i > \bar{\Omega}$, red arrows in Fig. 4) lead when the measured $S_z > 0$, and lag when $S_z < 0$:

$$\delta_i = \chi S_z (\Omega_i - \bar{\Omega}), \quad (2)$$

where $\chi \approx \frac{4\bar{\Omega}\langle n_1 \rangle}{\eta\kappa^2}$ is a constant that depends on the photon number per probe pulse (Appendix D). Thus, information about S_z is also imprinted in the atomic phase distribution in the equatorial plane. This information is usually not read out. For the timescales considered here, however, ISRE starts to play a role [25, 34]. Its action can be described by a kinetic equation which in its simplest form reads

$$\partial_t \mathbf{s}_i(\mathbf{E}, t) \approx \omega_{\text{ex}} \mathbf{S} \times \mathbf{s}_i(\mathbf{E}, t), \quad (3)$$

where $\mathbf{s}_i = \langle \hat{\mathbf{s}}_i \rangle$ and $\mathbf{S} = \langle \hat{\mathbf{S}} \rangle$ as defined earlier, are the spin vectors of individual spin and the collective spin respectively. \mathbf{s}_i is assumed to depend only on an atom's

motional energy $\mathbf{E} = \{E_x, E_y, E_z\}$. This is a reasonable approximation here, as the light-induced phase shift depends on the motional state. The initial distribution $\mathbf{s}_i(\mathbf{E})$ is determined by Eq. 2 and we neglect other sources of dephasing (such as the trapping potential), which become relevant on still longer timescales. The effect of ISRE is then to rotate the individual spins about their sum (Fig. 4, right column). The rotation rate is determined by ω_{ex} , and by $|\mathbf{S}|$ which is characterized by \mathcal{C} . While the total S_z is conserved, the s_z values of individual atoms evolve as

$$s_{z,i}(t) = s_z^0 + \frac{\delta_i}{2} \sin \mathcal{C} \omega_{\text{ex}} t. \quad (4)$$

The initial value is close to $s_z^0 = S_z/N$ for all atoms due to the QND measurement, and the plus sign is determined by the relevant scattering lengths in ^{87}Rb [35]. For times $t < \pi/(\mathcal{C}\omega_{\text{ex}})$, the strongly-coupled atoms now have above-average s_z if $S_z > 0$ was measured, and below-average s_z if $S_z < 0$. As these atoms will make an above-average contribution to M_2 , the result is an amplification of the measurement. Indeed, we obtain from the above equations

$$\delta\omega(t) = \sum_i^N \Omega_i s_{z,i}(t) = \bar{\Omega} S_z (1 + a_m \sin \mathcal{C} \omega_{\text{ex}} t), \quad (5)$$

where $a_m = \chi N (\Delta\Omega)^2 / 2\bar{\Omega}$ and $(\Delta\Omega)^2 = \frac{1}{N} \sum_i^N (\Omega_i - \bar{\Omega})^2$ is the variance of the coupling. $\alpha(t) = 1 + a_m \sin \mathcal{C} \omega_{\text{ex}} t$ is the time-dependent amplification factor. We thus expect an amplification that depends on the atom number, probe photon number, and coupling inhomogeneity, and increases for $t \lesssim \pi/(2\mathcal{C}\omega_{\text{ex}})$. While this simplified model predicts an oscillation of $\alpha(t)$, we expect it to damp out for times approaching the lateral collision timescale, as these collisions destroy the correlation between motional and internal state.

We have used this model in a Monte-Carlo simulation, where the initial atomic positions and velocities are randomly chosen according to the experimentally measured distributions (Appendix E). All parameters are chosen as in the experiment and there are no free parameters. The ISRE is modelled using a mean-field kinetic equation similar to previous work [25, 26, 34, 36]. Lateral collisions are accounted for by an exponential spin relaxation at the collision rate γ_c . The grey curve in Fig. 3(b) shows the simulation result. In spite of its simplicity, the model correctly reproduces the initial rise of the amplification factor, with good agreement up to 300 ms, when α reaches its maximum. For longer times, the oscillation of Eq. 5 is damped in the simulation due to the inclusion of lateral collisions and atom loss. Nevertheless, the simulation still predicts several periods of oscillation, which are not observed in the experiment. This suggests an additional damping mechanism, which may be related to the entanglement in the initial state.

The model also predicts that a correlation should arise between the spin state and motional energy due to the

ISRE rotation which transforms phase shift into population difference. For example, when M_1 yields $S_z > 0$, ISRE converts the phase shift of colder atoms into an increased probability of being in $|\uparrow\rangle$, and that of hotter atoms into an increased probability of $|\downarrow\rangle$, for times $t < \pi/(\mathcal{C}\omega_{\text{ex}})$ (cf. Fig. 4). For $S_z < 0$, $|\uparrow\rangle$ and $|\downarrow\rangle$ are reversed. More quantitatively, with Eqs. 2 and 4 one finds (Appendix D)

$$T_{t,\uparrow} \approx T(1 + a_T S_z \sin \mathcal{C}\omega_{\text{ex}} t), \quad (6)$$

and similarly $T_{t,\downarrow} \approx T(1 - a_T S_z \sin \mathcal{C}\omega_{\text{ex}} t)$, with a constant $a_T \approx \chi\Delta\Omega$. Here T_t is the temperature along the transverse axes. Thus, we find that the final transverse temperature should correlate with the measured S_z for $0 < t < \pi/(\mathcal{C}\omega_{\text{ex}})$. Eq. 6 also predicts that the fluctuation $\Delta T_{t,\uparrow(\downarrow)}$ should have a time evolution similar to that of the amplification factor (cf. Eq. 5), given the quantum fluctuations $\Delta S_z = \sqrt{N}/2$ of the initial state.

State-resolved time-of-flight imaging allows us to test this prediction. Our imaging system can resolve temperature changes below 10 nK in the \hat{z} direction. State sensitivity is achieved by state-selective outcoupling using microwave adiabatic passage [37]. In Fig. 5, we show the result of such temperature measurements, for the same dataset as in Fig. 3. We indeed observe the expected correlation between T_z and measured S_z when $\alpha > 0$ (Fig. 5(a)). Also, the fluctuation $\Delta T_{z,\uparrow}$ (open diamonds in (b)) follows the evolution of the amplification factor (blue circles, right axis) for times up to ~ 1 s. The observation of these nontrivial correlations provides further evidence that the simple ISRE model captures some essential features of the spin dynamics of the interacting spin-squeezed state.

IV. SQUEEZING LIFETIME

We now return to the question of the lifetime of the squeezed state. While our simple ISRE model predicts that the mean value of S_z should remain unmodified, the model cannot be used to predict its quantum fluctuations. However, more complete quantum models describe similar phenomena using an $\hat{\mathbf{S}} \cdot \hat{\mathbf{S}}$ term which commutes with \hat{S}_z [38], suggesting that ISRE dynamics may be compatible with spin squeezing.

Experimentally, we have already seen (Fig. 3) that the strong correlation between M_1 and M_2 persists over long times. Combining this data with independently measured coherence for different T_d (inset in Fig. 6), and employing again Eq. 1 to evaluate the conditional squeezing at the moment of M_2 in the presence of amplification, we obtain the time evolution of the metrological squeezing (Fig. 6). The data show that the state remains squeezed up to $T_d \approx 1$ s. At this time, background gas collisions have already reduced the atom number by 28%. For an ideal two-mode symmetric squeezed state, one-body loss reduces spin squeezing according to $(\xi_N^2 - 1)(t) = (\xi_N^2 - 1)(0)e^{-\gamma t}$ [39], where ξ_N is the number

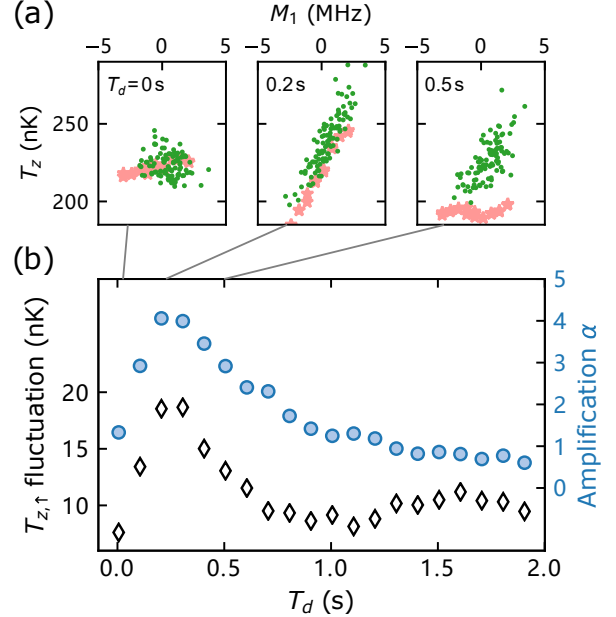


FIG. 5. Additional evidence of ISRE in the amplification data. (a) Raw data (green dots) of temperature versus M_1 at times $T_d = 0, 0.2, 0.5$ s, showing that T_z is well correlated with S_z when $\alpha > 0$. Red stars shows the simulation results (same as Fig. 3(b)), which well predict the correlation at short times. A 20 nK offset has been applied to the simulation data to account for a bias in the temperature measurement. (b) The fluctuation (standard deviation) of T_z for $|\uparrow\rangle$ (open diamonds) has a time evolution resembling the amplification factor (blue circles, same data as in Fig. 3).

squeezing factor and $1/\gamma = 3.0(1)$ s is our trap lifetime. The measured squeezing exceeds this expected squeezing for $0.2 < T_d < 0.8$ s, which coincides with the period in which α is significantly greater than unity. The quantum correlations created by the amplification effect may play a role in explaining this discrepancy.

V. CONCLUSION

The amplification effect is similar in its result, but very different in its mechanism, from recently demonstrated “quantum phase magnification” protocols [40, 41] and mechanical counterparts [42]. These protocols work by inserting a well-engineered unitary evolution between the sensing phase and the detection such that the spin observable itself is magnified to facilitate detection. In our scheme, the collective S_z does not change its expectation value. Instead, the cavity measurement is amplified due to a correlation between spin and motional states, leading to a spin-dependent detectivity. The mechanism thus provides a novel scheme for improving the resolution of cavity-based spin squeezing measurement, reducing noise for a given number of detected photons, or achieving the same resolution with less probe photons and hence less

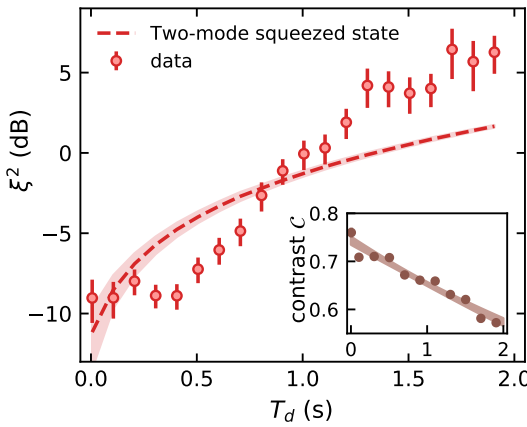


FIG. 6. Inferred metrological squeezing as a function of time T_d , given by the conditional noise (Eq. 1) normalized to the SQL (here $N = 2.1(1) \times 10^4$) and coherence at T_d . The dashed curve represents the expected squeezing decay of an ideal, two-mode squeezed state under one-body atom loss, with the initial squeezing given by the theoretical PSN limit, also normalized to the experimental coherence. The inset shows the evolution of the measured contrast (circles) and an exponential fit (shaded line, width indicating fit uncertainty) which yields $\tau = 7.7(6)$ s.

destructivity.

We gained an initial understanding of the effect with a simple model that involves the motional energy of atoms as a “memory” of the spin correlations. A more complete model should take into account the quantum correlations in the collective spin state, which are established before exchange dynamics sets in, and modify this dynamics. The same ingredients are present in other interacting spin systems, where they can lead to non-trivial many-body physics [28, 43, 44].

The experimental results for long-lived spin squeezing on a microwave clock transition raise hopes for a squeezing-enhanced clock with metrologically relevant long Ramsey time in the near future. The observed spin interaction effect not only preserves the reduced spin noise but also facilitates detection due to a subtle amplification effect. More generally, these results emphasize the importance of many-body atomic interactions for quantum-enhanced metrology.

Note added While preparing this manuscript, we became aware of a recent preprint [45] describing spin squeezing in an optical clock with noise reduction up to two hundred milliseconds.

VI. ACKNOWLEDGEMENTS

We thank Jean-Noël Fuchs, Frédéric Piéchon and Franck Laloë for fruitful discussions, and also thank JNF for assistance with the numerical simulation. We acknowledge early contributions to the setup from Ralf Kohlhaas and Théo Laudat and are indebted to Tobias

Gross of Laseroptik GmbH for advice on the fiber mirror coatings. This work is supported by the European Research Council (ERC) (Advanced Grant 671133 EQUEMI), by the Délégation Générale de l’Armement (DGA) via the ANR ASTRID program (Contract No. ANR-14-ASTR-0010) and by Région Ile-de-France (DIM SIRTEQ).

Appendix A: Experimental Details

1. Set-up and parameters

The layout of the atom chip and details of the two-photon clock transition are shown in Fig. 7. The microwave (MW) photon is detuned 454 kHz above the $|\downarrow\rangle \rightarrow |F = 2, m_F = 0\rangle$ transition and delivered by an on-chip coplanar waveguide, the radiofrequency (RF) photon from another chip wire. After magneto-optical trapping, optical molasses and optical pumping to $|\downarrow\rangle$, atoms are magnetically trapped at the MOT site and magnetically transported to the cavity using the “omega wire” (Fig. 7), where the trap is compressed and forced RF evaporative cooling is applied. Finally, the trap is decompressed to its final parameters (“interrogation trap”) and positioned exactly inside the optical cavity mode. Due to the low density, the final state is not completely thermalized and has a slight temperature difference between the longitudinal and transverse axes, as quoted in the main text. The complete loading and preparation phase takes 3 s. In the interrogation trap, the magnetic field at the bottom of the trap points along \hat{x} and has a value $B_x = B_m - 35$ mG, where $B_m = 3.229$ G is the “magic” field for which the linear differential Zeeman shift between the clock states vanishes [31] and the 35 mG offset maximizes coherence time [25].

The state-resolved imaging starts with a MW pulse that adiabatically transfers atoms from $|\downarrow\rangle$ to $|F = 2, m_F = 0\rangle$, where they are no longer trapped and start to fall. The trap is turned off several milliseconds later to release atoms in $|\uparrow\rangle$, such that the two clouds are well separated and are imaged in a single picture. However, the adiabatic transfer also perturbs the trap so that the temperature estimation is slightly biased.

The optical cavity is symmetric with a finesse $\mathcal{F} = 2.7(1) \times 10^3$ for the 780 nm mode. This gives a maximum single-atom cooperativity $C_0 = 24\mathcal{F}/\pi k_{780}^2 w_0^2 \approx 1.9$, where k_{780} is the wave vector of the probe laser. Taking into account the inhomogeneity for our trapped cloud with $T \sim 200$ nK, the effective cooperativity is $C_{\text{eff}} \approx 0.42$. The cavity is simultaneously resonant for a stabilization wavelength at 1560 nm. The stabilization laser is constantly on during the experiment, but its intra-cavity intensity is sufficiently weak in order not to trap the atoms (trap depth $\lesssim 20$ nK).

2. Calibrations

The imaging system is calibrated using the known \sqrt{N} scaling of the projection noise of a coherent state, similar to [13]. To measure $\bar{\Omega}$, we prepare CSSs with different $\langle S_z \rangle$ by applying a weak MW+RF pulse of variable length. Cavity transmission spectra are obtained by scanning a weak probe laser over 20 cavity linewidths in 50 ms. We obtain the prepared $\langle S_z \rangle$ from the imaging data. A linear fit of cavity frequency versus prepared $\langle S_z \rangle$ yields $\bar{\Omega}$. Our preparation procedure leads to a small dependence between temperature and the prepared atom number. Therefore, the measured $\bar{\Omega}$ slightly depends on N (1.5% deviation for 10% change in N).

We calibrate the phase shift induced by the cavity probe using a Ramsey sequence (with the probe pulse occurring during the Ramsey time). We obtain the ensemble-average phase shift per detected photon $\bar{\phi}_d = 4.16(2) \times 10^{-4} \pi$ rad. Ideally, for a given atom i , the phase shift is given by $\phi_i = \frac{\Omega_i}{\kappa_t} n_t$, where n_t is the transmitted photon number and $\kappa_t = \mathcal{T}c/(2L) \lesssim \kappa/2$ is the transmission rate, with $\mathcal{T} = 1000$ ppm the designed mirror transmission and c the speed of light. This allows us to estimate the overall photon detection efficiency η by comparing $\bar{\phi}_d$ with the expected phase shift per transmitted photon ($\langle \phi_i \rangle / n_t = \bar{\Omega}/\kappa_t$).

3. Composite cavity measurement

We defined the composite cavity measurement $M_l = (\delta\omega_{l+} - \delta\omega_{l-})/2$ ($l = 1, 2$). In order to account for the π pulses that flip S_z , we define $\delta\omega_{\pm}$ accordingly, such that $\delta\omega_+$ ($\delta\omega_-$) refers to the second (first) probe for M_1 , but refers to the first (second) probe for M_2 (see Fig. 1(d)). Consequently, S_z refers to the state after M_1 .

We obtain the cavity shifts $\delta\omega_{\pm}$ from the transmitted photon number, taking into account the Lorentzian line shape. At the end of each experimental cycle (after atoms are imaged), we apply two additional cavity probe pulses with $\pm\kappa/2$ detuning, to calibrate possible long term drift of the cavity frequency and the probe intensity.

Experimentally, we employ a SCROFULOUS composite π pulse [46], with each of the constituent pulses tuned to a duration of the transverse trap period $2\pi/\omega_z$. This helps to reduce the pulse error due to amplitude inhomogeneity and fluctuation.

Appendix B: Inhomogeneous coupling

The atom-field coupling in the cavity is a function of atomic trajectory $\mathbf{r}(t) = \{x, y, z\}$, and is determined by the cavity geometry,

$$\Omega(\mathbf{r}) = \Omega_0 \cos^2(k_{780}x) \left(\frac{w_0}{w}\right) \exp\left[-2\frac{y^2 + z^2}{w^2}\right], \quad (B1)$$

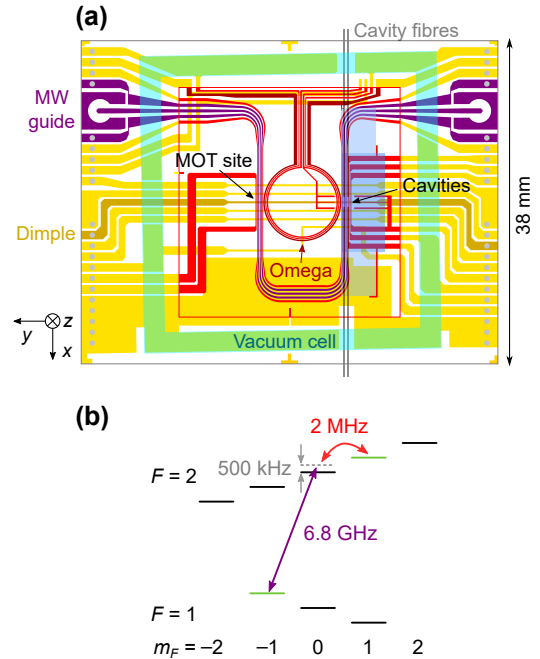


FIG. 7. (a) Layout of the atom chip, which has a two-layer structure and incorporates two fiber Fabry-Perot (FFP) cavities of different finesse. Only the low-finesse cavity (located left in the image) is used in the experiments described here. Red (yellow) wires are on the top (bottom) chip. The central “Omega” wire is used to transfer atoms from the MOT site to the cavity. Green shade indicates the cross-section of the vacuum cell. (b) Zeeman levels of the ⁸⁷Rb ground state. Clock states are marked in green. The clock transition is excited with two-photon pulses as indicated.

where $w = w_0 \sqrt{1 + x^2/L_R^2}$ with $L_R = k_{780}w_0^2/2 \approx 750 \mu\text{m}$ the Rayleigh length. The maximum shift Ω_0 can be obtained from the experimentally measured $\bar{\Omega}$, and agrees with the value obtained from a cavity quantum electrodynamics calculation. The time integral of $\Omega(\mathbf{r})$ over the pulse duration τ_p yields the effective coupling $\Omega_i = \frac{1}{\tau_p} \int_0^{\tau_p} dt \Omega(\mathbf{r}_i)$ for atom i used in the main text. Assuming harmonic oscillation, the position dependence in the transverse directions reduces to a function of the motional energies $E_{y,i}$ and $E_{z,i}$:

$$\Omega_i \approx \Omega_0 \left(1 - \frac{x_i^2}{L_R^2}\right) e^{-\left(\frac{E_{y,i}}{\varepsilon_y} + \frac{E_{z,i}}{\varepsilon_z}\right)} I_0\left(\frac{E_{y,i}}{\varepsilon_y}\right) I_0\left(\frac{E_{z,i}}{\varepsilon_z}\right) \quad (B2)$$

where $\varepsilon_y \equiv \frac{m\omega_y^2 w_0^2}{2}$ and $\varepsilon_z \equiv \frac{m\omega_z^2 w_0^2}{2}$. In the experiment, the averaging is not perfect along \hat{y} since ω_y and ω_z are not precisely equal. $I_0(\cdot)$ is the modified Bessel function of the first kind. Note that we assume the standing wave in \hat{x} can be averaged out and the position dependence on x is weak as the cloud size $\ll L_R$. As a result, as in most real systems, atoms contribute differently to the quantum fluctuations of $\delta\omega = \bar{\Omega}S_z$. Nevertheless, the system can be described like a uniformly coupled one with a slightly

reduced effective atom number $N_{\text{eff}} = \frac{(\sum_i^N \Omega_i)^2}{\sum_i^N \Omega_i^2}$ and coupling $\Omega_{\text{eff}} = \frac{\sum_i^N \Omega_i^2}{\sum_i^N \Omega_i}$, as long as the couplings do not change over time [12, 32]. Note that as $N_{\text{eff}} \Omega_{\text{eff}} = N \bar{\Omega}$ and $\xi^2 = 4(\Delta S_z)^2 |_{M_1}/(N\mathcal{C}^2) \propto 1/N\bar{\Omega}^2$ (Eq. 1), the squeezing will appear higher if N_{eff} and Ω_{eff} are used. For our system, $N_{\text{eff}} \approx 0.90N$ and $\Omega_{\text{eff}} \approx 1.11\bar{\Omega}$, so that the effect on ξ is within 10%. We have used N (measured by imaging) and $\bar{\Omega}$ to obtain a conservative estimate of the squeezing.

Appendix C: Data analysis

1. Coherence measurements

To determine the atomic coherence after a composite measurement (Fig. 2(b) and Fig. 6 inset), we apply a second $\pi/2$ pulse after M_1 , effectively forming a Ramsey sequence with M_1 occurring during the Ramsey time. By varying the phase of the second $\pi/2$ pulse, we obtain Ramsey fringes (S_z versus phase). However, M_1 induces an average phase shift depending on the measured S_z value, which fluctuates from shot to shot due to quantum projection noise. We correct this phase shift in the data analysis using the calibrated phase shift per detected photon (Appendix A 2) and the number of detected photons in M_1 in each shot. We can then obtain the contrast with a sinusoidal fit of the Ramsey fringes.

We fit the contrast decay as a function of average detected photons to $\mathcal{C} = \exp[-\langle n_1 \rangle/\gamma_1 - (\langle n_1 \rangle/\gamma_2)^2]$ (Fig. 2(b)), yielding $\gamma_1 = 3(1) \times 10^5 \gg \gamma_2 = 1.88(7) \times 10^4$. The second term dominates, which can be understood as follows: the imperfection in the spin echo compensation leads to a Gaussian distribution of the atomic phase, whose width depends linearly on the measurement strength ($\langle n_1 \rangle$). This gives the dominant scaling $\mathcal{C} \propto \exp[-\langle n_1 \rangle^2]$.

2. Conditional noise

We infer the conditional spin noise from the conditional variance of M_2 : $\text{Var}(M_1 - M_2/\alpha)$. Mathematically, $\text{Var}(M_1 - M_2/\alpha)$ is minimized with $1/\alpha = \text{Cov}(M_1, M_2)/\text{Var}(M_2)$, equivalent to the slope of a simple linear regression between M_1 and M_2 (M_2 is the independent variable). However, given that there is PSN both in M_1 and M_2 , the simple linear regression gives a biased slope. More accurate is an orthogonal regression allowing errors in both variables (“Deming regression”). It is equivalent to minimizing $\frac{\text{Var}(M_1 - M_2/\alpha)}{(\Delta M_1^{\text{PSN}})^2 + (\Delta M_2^{\text{PSN}})^2/\alpha^2}$, which is the conditional variance normalized to the PSN. We obtain α in this way for the data shown in Fig. 2 and 3. Clearly, in the presence of amplification, $\alpha > 1$: the PSN of M_2 contributes less to the conditional noise due to the factor $1/\alpha^2$.

3. Spin tomography

ΔS_θ^2 is also estimated in a conditional way similar to Eq. 1 (as in [16]):

$$(\Delta S_z)_\theta^2 \leq [\text{Var}(M_1 \cos \theta - M_2) - (\Delta M_2^{\text{PSN}})^2] / \bar{\Omega}^2. \quad (\text{C1})$$

The data shown in Fig. 2(c) are after a post-selection of the measured S_z (close to 0), because with our composite measurement scheme the shot-to-shot phase fluctuation is dominated by the quantum fluctuation of S_z (see Eq. D1 below). In principle, this phase fluctuation can be suppressed by an active feedback on the phase based on the cavity measurement result, up to the ultimate PSN. Post-selection simulates the optimal situation with active feedback, while the discrepancy between the data and the prediction (pink curve) comes from the fact that the post-selection is not stringent due to the limited number of samples. With an optimal phase feedback, PSN induces at least 6.1 dB excess anti-squeezing, which needs to be taken into account in real clock applications [33]. It is worth noting that cavity feedback squeezing [11] which can enable near unitary squeezing [47] can also be implemented in our system.

Appendix D: Amplification model

Here we formulate the simple model (Eqs. 2–6) in more detail. We make the following assumptions: 1) Ω_i is only determined by $E_{y,i}$ and $E_{z,i}$, which are conserved during the experiment (Eq. B2). The ensemble coupling $\bar{\Omega} = \frac{1}{N} \sum_i^N \Omega_i$ is then a constant; 2) the spin rotation is modeled as a simple rotation of each spin around the ensemble average with the same rate $\mathcal{C}\omega_{\text{ex}}$, determined by the atomic coherence ($|\mathbf{S}|$ in Eq. 3). We ignore other sources of dephasing, such as dephasing from the trapping potential; 3) we also assume a perfect π pulse on the clock transition for the spin echo and no spin dynamics during the composite measurement.

The phase shift induced by M_1 is obtained from the transmitted photon numbers $n_{1\pm}$ in the two probe pulses. With a linear approximation of the cavity transmission (probe detuning $\kappa/2$), $n_{1\pm} \approx n_p(1 + 2\delta\omega_{1\pm}/\kappa)$, where n_p is the average transmitted photon number per probe pulse (an experimental parameter), $n_p = \langle n_1 \rangle/(2\eta)$, and $\langle n_1 \rangle$ is the average detected photon number in M_1 used in the main text. According to our sign convention (Appendix A 3), the first probe gives $\phi_{i-} = \frac{\Omega_i}{\kappa_t} n_p \left(1 - \frac{2\bar{\Omega}}{\kappa} S_z\right)$ (note the minus sign of S_z), which acquires a minus sign after the spin echo pulse. The second probe gives $\phi_{i+} = \frac{\Omega_i}{\kappa_t} n_p \left(1 + \frac{2\bar{\Omega}}{\kappa} S_z\right)$ and the total phase shift in M_1 reads

$$\phi_i = \phi_{i+} - \phi_{i-} = \frac{4\bar{\Omega}n_p}{\kappa_t\kappa} \Omega_i S_z \quad (\text{D1})$$

The phase deviation from the mean phase $\bar{\phi} = \arctan(\sum_i \sin(\phi_i)/\sum_i \cos(\phi_i)) \approx \frac{1}{N} \sum_i \phi_i$ is then $\delta_i = \phi_i - \bar{\phi} = \chi S_z(\Omega_i - \bar{\Omega})$ with $\chi = \frac{4\Omega n_p}{\kappa_t \kappa} \approx \frac{4\bar{\Omega}\langle n_1 \rangle}{\eta \kappa^2}$ (Eq. 2). Eq. 4 and Eq. 5 then follow.

To obtain Eq. 6, we consider the motional energy $E_{t,i}$ of atom i in the transverse directions ($t = y, z$). Ω_i is a monotonically decreasing function of $E_{t,i}$ (see Eq. B2) and here we approximate it by $\Omega_i - \bar{\Omega} \approx -\varepsilon(E_{t,i} - \bar{E}_t)$, where $\bar{E}_t = \frac{1}{N} \sum_i^N E_{t,i} = k_B T$ and ε is a positive constant. It follows that $\text{Var}(\Omega) \approx \varepsilon^2 \text{Var}(E_t) = \varepsilon^2 (k_B T)^2$, so $\varepsilon = \Delta\Omega/k_B T$. Overall, the average energy of $|\uparrow\rangle$ can be written as $E_{t,\uparrow} \approx \frac{1}{N_\uparrow} \sum_i^N P_{\uparrow,i} E_{t,i}$, where $P_{\uparrow,i} = \frac{1}{2} - s_{z,i}$ and $N_\uparrow = \sum_i^N P_{\uparrow,i} = N/2 - S_z$ (similar for $|\downarrow\rangle$ with $P_{\downarrow,i} = \frac{1}{2} + s_{z,i}$). Note the replacement $s_z \rightarrow -s_z$ due to the final base change (π pulse) in M_2 . ISRE furthermore correlates $s_{z,i}$ with $E_{t,i}$ through Ω_i . Using Eq. 4, after an evolution time t ,

$$\begin{aligned} E_{t,\uparrow} &\approx \frac{2}{N - 2S_z} \sum_i^N \left(\frac{1}{2} - s_{z,i} \right) E_{t,i} \\ &\approx \bar{E}_t + \frac{\chi S_z \sin \mathcal{C} \omega_{\text{ext}} t}{N - 2S_z} \sum_i^N \varepsilon(E_{t,i} - \bar{E}_t) E_{t,i} \\ &\approx k_B T + \chi \varepsilon (k_B T)^2 S_z \sin \mathcal{C} \omega_{\text{ext}} t \end{aligned} \quad (\text{D2})$$

where we have used $N \gg S_z$; and $\text{Var}(E_t) = (k_B T)^2$ for thermal distribution. The experimentally measured transverse temperature directly links to the average energy as $T_{t,\uparrow(\downarrow)} \approx E_{t,\uparrow(\downarrow)}/k_B$. This leads to Eq. 6 with $a_T = \chi \Delta\Omega$.

Appendix E: Numerical simulation

To better understand the amplification effect including lateral collisions and residual dephasing from the magnetic trap, we perform numerical simulations of

the spin dynamics using a semi-classical kinetic equation for the spin vector \mathbf{s} in the space of motional energies $\mathbf{E} = \{E_x, E_y, E_z\}$ [25, 34]:

$$\begin{aligned} \partial_t \mathbf{s}(\mathbf{E}, t) + \gamma_c [\mathbf{s}(\mathbf{E}, t) - \bar{\mathbf{s}}] \\ = \left[\delta\omega_a(\mathbf{r}(t), t) \mathbf{e}_z + \omega_{\text{ex}} \int_0^\infty d\mathbf{E}' \beta^3 e^{-\beta \mathbf{E}'} K(\mathbf{E}, \mathbf{E}') \mathbf{s}(\mathbf{E}', t) \right] \\ \times \mathbf{s}(\mathbf{E}, t) \end{aligned} \quad (\text{E1})$$

where $\bar{\mathbf{s}} \equiv \int_0^\infty d\mathbf{E} \beta^3 e^{-\beta \mathbf{E}} \mathbf{s}(\mathbf{E})$ describes the average spin. Integration is done on all three energies. \mathbf{e}_z is the unit vector \hat{z} in the Bloch sphere, generating spin precession at rate $\delta\omega_a(\mathbf{r}, t)$ which includes three dephasing sources: AC Stark shift induced by the cavity probe (see Eq. B1), shifts due to the magnetic trap and mean-field collisions [29]. We include the spatial dependence of $\delta\omega_a$ to account for imperfections in the trap oscillation averaging (cf. Eq. B2). The spin interaction depends on ω_{ex} as well as the spin “mean field”, and is long-ranged in energy space (Knudsen regime), described by the kernel $K(\mathbf{E}, \mathbf{E}')$ which we will approximate with $K(\mathbf{E}, \mathbf{E}') \approx 1$ [25, 36] (this approximation slightly augments the exchange rate). The lateral collision rate γ_c is incorporated as a relaxation toward the mean spin.

To perform numerical Monte-Carlo simulations, we randomly sample the position and momentum of $\sim 10^4$ atoms in a thermal distribution. The coordinates $\mathbf{r}(t)$ evolve as in pure harmonic oscillation. The atoms then have well defined energies along each axis. The cavity shift at each time step is calculated as $\sum_i \Omega(\mathbf{r}_i(t)) s_{z,i}(t)$ according to Eq. B1 with each atom’s s_z component. In order to simulate the amplification effect which amplifies quantum fluctuations in S_z , we start with all atoms having a common s_z component that deviates from 0 (a classical approximation to the result of a QND cavity measurement, as in Fig. 4). From the subsequently calculated cavity shift over time, we can obtain M_1 and M_2 hence their ratio α .

[1] M. Kitagawa and M. Ueda, Squeezed spin states, *Physical Review A* **47**, 5138 (1993).

[2] D. J. Wineland, J. J. Bollinger, W. M. Itano, and D. J. Heinzen, Squeezed atomic states and projection noise in spectroscopy, *Physical Review A* **50**, 67 (1994).

[3] J. Ma, X. Wang, C. P. Sun, and F. Nori, Quantum spin squeezing, *Physics Reports* **509**, 89 (2011).

[4] L. Pezzè, A. Smerzi, M. K. Oberthaler, R. Schmied, and P. Treutlein, Quantum metrology with nonclassical states of atomic ensembles, *Reviews of Modern Physics* **90**, 035005 (2018).

[5] G. Santarelli, P. Laurent, P. Lemonde, A. Clairon, A. G. Mann, S. Chang, A. N. Luiten, and C. Salomon, Quantum projection noise in an atomic fountain: A high stability cesium frequency standard, *Physical Review Letters* **82**, 4619 (1999).

[6] E. Oelker, R. B. Hutson, C. J. Kennedy, L. Sonderhouse, T. Bothwell, A. Goban, D. Kedar, C. Sanner, J. M. Robinson, G. E. Marti, D. G. Matei, T. Legero, M. Giunta, R. Holzwarth, F. Riehle, U. Sterr, and J. Ye, Demonstration of 4.8×10^{-17} stability at 1 s for two independent optical clocks, *Nature Photonics* **13**, 714 (2019).

[7] G. Rosi, F. Sorrentino, L. Cacciapuoti, M. Prevedelli, and G. M. Tino, Precision measurement of the newtonian gravitational constant using cold atoms, *Nature* **510**, 518 (2014).

[8] B. Barrett, A. Bertoldi, and P. Bouyer, Inertial quantum sensors using light and matter, *Physica Scripta* **91**, 053006 (2016).

[9] W. Wasilewski, K. Jensen, H. Krauter, J. J. Renema, M. V. Balabas, and E. S. Polzik, Quantum noise limited and entanglement-assisted magnetometry, *Physical*

Review Letters **104**, 133601 (2010).

[10] J. Appel, P. J. Windpassinger, D. Oblak, U. B. Hoff, N. Kjaergaard, and E. S. Polzik, Mesoscopic atomic entanglement for precision measurements beyond the standard quantum limit, *Proceedings of the National Academy of Sciences* **106**, 10960 (2009).

[11] I. D. Leroux, M. H. Schleier-Smith, and V. Vuletić, Implementation of cavity squeezing of a collective atomic spin, *Physical Review Letters* **104**, 073602 (2010).

[12] M. H. Schleier-Smith, I. D. Leroux, and V. Vuletić, States of an ensemble of two-level atoms with reduced quantum uncertainty, *Physical Review Letters* **104**, 073604 (2010).

[13] M. F. Riedel, P. Böhi, Y. Li, T. W. Hänsch, A. Sinatra, and P. Treutlein, Atom-chip-based generation of entanglement for quantum metrology, *Nature* **464**, 1170 (2010).

[14] C. Gross, T. Zibold, E. Nicklas, J. Estève, and M. K. Oberthaler, Nonlinear atom interferometer surpasses classical precision limit, *Nature* **464**, 1165 (2010).

[15] J. G. Bohnet, K. C. Cox, M. A. Norcia, J. M. Weiner, Z. Chen, and J. K. Thompson, Reduced spin measurement back-action for a phase sensitivity ten times beyond the standard quantum limit, *Nature Photonics* **8**, 731 (2014).

[16] K. C. Cox, G. P. Greve, J. M. Weiner, and J. K. Thompson, Deterministic squeezed states with collective measurements and feedback, *Physical Review Letters* **116**, 093602 (2016).

[17] J. G. Bohnet, B. C. Sawyer, J. W. Britton, M. L. Wall, A. M. Rey, M. Foss-Feig, and J. J. Bollinger, Quantum spin dynamics and entanglement generation with hundreds of trapped ions, *Science* **352**, 1297 (2016).

[18] O. Hosten, N. J. Engelsen, R. Krishnakumar, and M. A. Kasevich, Measurement noise 100 times lower than the quantum-projection limit using entangled atoms, *Nature* **529**, 505 (2016).

[19] I. D. Leroux, M. H. Schleier-Smith, and V. Vuletić, Orientation-dependent entanglement lifetime in a squeezed atomic clock, *Physical Review Letters* **104**, 250801 (2010).

[20] R. J. Sewell, M. Koschorreck, M. Napolitano, B. Dubost, N. Behbood, and M. W. Mitchell, Magnetic sensitivity beyond the projection noise limit by spin squeezing, *Physical Review Letters* **109**, 253605 (2012).

[21] H. Bao, J. Duan, S. Jin, X. Lu, P. Li, W. Qu, M. Wang, I. Novikova, E. E. Mikhailov, K.-F. Zhao, K. Mølmer, H. Shen, and Y. Xiao, Spin squeezing of 1011 atoms by prediction and retrodiction measurements, *Nature* **581**, 159 (2020).

[22] J. Guéna, M. Abgrall, D. Rovera, P. Laurent, B. Chupin, M. Lours, G. Santarelli, P. Rosenbusch, M. E. Tobar, R. Li, K. Gibble, A. Clairon, and S. Bize, Progress in atomic fountains at LNE-SYRTE, *IEEE Transactions on Ultrasonics, Ferroelectrics and Frequency Control* **59**, 391 (2012).

[23] T. Bothwell, D. Kedar, E. Oelker, J. M. Robinson, S. L. Bromley, W. L. Tew, J. Ye, and C. J. Kennedy, JILA SrI optical lattice clock with uncertainty of 2.0×10^{-18} , *Metrologia* **56**, 065004 (2019).

[24] C. Lhuillier and F. Laloë, Transport properties in a spin polarized gas, i, *Journal de Physique* **43**, 197 (1982).

[25] C. Deutsch, F. Ramirez-Martinez, C. Lacroûte, F. Reinhard, T. Schneider, J. N. Fuchs, F. Piéchon, F. Laloë, J. Reichel, and P. Rosenbusch, Spin self-rephasing and very long coherence times in a trapped atomic ensemble, *Physical Review Letters* **105**, 020401 (2010).

[26] C. Solaro, A. Bonnin, F. Combes, M. Lopez, X. Alauze, J.-N. Fuchs, F. Piéchon, and F. Pereira Dos Santos, Competition between spin echo and spin self-rephasing in a trapped atom interferometer, *Physical Review Letters* **117**, 163003 (2016).

[27] S. L. Bromley, S. Kolkowitz, T. Bothwell, D. Kedar, A. Safavi-Naini, M. L. Wall, C. Salomon, A. M. Rey, and J. Ye, Dynamics of interacting fermions under spin-orbit coupling in an optical lattice clock, *Nature Physics* **14**, 399 (2018).

[28] S. Smale, P. He, B. A. Olsen, K. G. Jackson, H. Sharum, S. Trotzky, J. Marino, A. M. Rey, and J. H. Thywissen, Observation of a transition between dynamical phases in a quantum degenerate fermi gas, *Science Advances* **5**, eaax1568 (2019).

[29] R. Szmuk, V. Dugrain, W. Maineult, J. Reichel, and P. Rosenbusch, Stability of a trapped-atom clock on a chip, *Physical Review A* **92**, 012106 (2015).

[30] K. Ott, S. Garcia, R. Kohlhaas, K. Schüppert, P. Rosenbusch, R. Long, and J. Reichel, Millimeter-long fiber fabry-perot cavities, *Optics Express* **24**, 9839 (2016).

[31] D. M. Harber, H. J. Lewandowski, J. M. McGuirk, and E. A. Cornell, Effect of cold collisions on spin coherence and resonance shifts in a magnetically trapped ultracold gas, *Physical Review A* **66**, 053616 (2002).

[32] J. Hu, W. Chen, Z. Vendeiro, H. Zhang, and V. Vuletić, Entangled collective-spin states of atomic ensembles under nonuniform atom-light interaction, *Physical Review A* **92**, 063816 (2015).

[33] B. Braverman, A. Kawasaki, and V. Vuletić, Impact of non-unitary spin squeezing on atomic clock performance, *New Journal of Physics* **20**, 103019 (2018).

[34] F. Piéchon, J. N. Fuchs, and F. Laloë, Cumulative identical spin rotation effects in collisionless trapped atomic gases, *Physical Review Letters* **102**, 215301 (2009).

[35] J. N. Fuchs, D. M. Gangardt, and F. Laloë, Internal state conversion in ultracold gases, *Physical Review Letters* **88**, 230404 (2002).

[36] S. Pegahan, J. Kangara, I. Arakelyan, and J. E. Thomas, Spin-energy correlation in degenerate weakly-interacting fermi gases, *Physical Review A* **99**, 063620 (2019).

[37] T. Laudat, V. Dugrain, T. Mazzoni, M.-Z. Huang, C. L. G. Alzar, A. Sinatra, P. Rosenbusch, and J. Reichel, Spontaneous spin squeezing in a rubidium BEC, *New Journal of Physics* **20**, 073018 (2018).

[38] M. J. Martin, M. Bishof, M. D. Swallows, X. Zhang, C. Benko, J. von Stecher, A. V. Gorshkov, A. M. Rey, and J. Ye, A quantum many-body spin system in an optical lattice clock, *Science* **341**, 632 (2013).

[39] Y. Li, Y. Castin, and A. Sinatra, Optimum spin squeezing in bose-einstein condensates with particle losses, *Physical Review Letters* **100**, 210401 (2008).

[40] E. Davis, G. Bentsen, and M. Schleier-Smith, Approaching the heisenberg limit without single-particle detection, *Physical Review Letters* **116**, 053601 (2016).

[41] O. Hosten, R. Krishnakumar, N. J. Engelsen, and M. A. Kasevich, Quantum phase magnification, *Science* **352**, 1552 (2016).

[42] S. C. Burd, R. Srinivas, J. J. Bollinger, A. C. Wilson, D. J. Wineland, D. Leibfried, D. H. Slichter, and D. T. C. Allcock, Quantum amplification of mechanical oscillator motion, *Science* **364**, 1163 (2019).

- [43] M. A. Norcia, R. J. Lewis-Swan, J. R. K. Cline, B. Zhu, A. M. Rey, and J. K. Thompson, Cavity-mediated collective spin-exchange interactions in a strontium superradiant laser, *Science* **361**, 259 (2018).
- [44] E. J. Davis, G. Bentsen, L. Homeier, T. Li, and M. H. Schleier-Smith, Photon-mediated spin-exchange dynamics of spin-1 atoms, *Physical Review Letters* **122**, 010405 (2019).
- [45] E. Pedrozo-Peña, S. Colombo, C. Shu, A. F. Adiyatullin, Z. Li, E. Mendez, B. Braverman, A. Kawasaki, D. Akamatsu, Y. Xiao, and V. Vuletić, Entanglement-enhanced optical atomic clock, arXiv 2006.07501 (2020).
- [46] H. K. Cummins, G. Llewellyn, and J. A. Jones, Tackling systematic errors in quantum logic gates with composite rotations, *Physical Review A* **67**, 042308 (2003).
- [47] B. Braverman, A. Kawasaki, E. Pedrozo-Peña, S. Colombo, C. Shu, Z. Li, E. Mendez, M. Yamoah, L. Salvi, D. Akamatsu, Y. Xiao, and V. Vuletić, Near-unitary spin squeezing in Yb171, *Physical Review Letters* **122**, 223203 (2019).